Three-dimensional critical behavior and anisotropic magnetic entropy change in the axion insulator candidate EuSn$_2$P$_2$

Xiaojun Yang [ORCID],[*] Junxiao Pan, Xiangyu He, Leiming Cao, Yan Cao, and Yaping Tao [ORCID]

College of Physics and Electronic Information, Luoyang Normal University, Luoyang 471022, China

The magnetic properties of the axion insulator candidate EuSn$_2$P$_2$ are comprehensively investigated. Under an applied external field, the antiferromagnetic phase below 30 K is driven to a forced ferromagnetic state. The yielded Rhodes-Wolfarth ratio (RWR) is equal to 1.13 (1.12) with $H//ab$ ($H//c$), indicating the forced ferromagnetism in EuSn$_2$P$_2$ is weak itinerant. A large magnetocrystalline anisotropy with $K_u = 521$ kJ/m^3 at 2 K is evaluated. Analysis on the critical behavior generates a set of critical exponents $\beta = 0.281(2)$ with $T_C = 30.2(1)$ K, $\gamma = 0.77(3)$ with $T_C = 30.1(1)$ K, and $\delta = 3.76(4)$ at $T_C = 30$ K, exhibiting a three-dimensional critical behavior. A phase diagram of H versus T is established, where a tricritical point at temperature and field of (30 K, 16.7 kOe) is determined on the boundaries of the paramagnetic, antiferromagnetic, and forced ferromagnetic states. In addition, the magnetic entropy change exhibits anisotropic behavior. The maximal value of the magnetic entropy $-\Delta S_M^{max}$ reaches 7.36 (6.41) J kg^{-1} K^{-1} with a magnetic field change of 50 kOe in $H//ab$ ($H//c$), which is comparable with that of well-known materials suitable for magnetic refrigeration with second-order ferromagnetic transitions. The plots of $-\Delta S_M(T, H)$ of high field can be rescaled into a universal curve, verifying the high-field paramagnetic to forced ferromagnetic transition is of a second order. The well-established scaling behavior of the magnetization and the magnetic entropy change further supports EuSn$_2$P$_2$ as an axion insulator.

DOI: 10.1103/PhysRevB.107.054440

I. INTRODUCTION

Emerged as a frontier of condensed matter physics and material science, topological materials have drawn researchers' attention due to the rich quantum phases and possible applications in future quantum computations and dissipationless topological electronics [1–3]. Among them, intrinsic magnetic topological materials are of essential interest owing to the prospective applications in spintronic devices. Compared to dilute magnetic topological insulators [4], intrinsic magnetic materials are stoichiometric magnetic compounds, offering a tunable, easily synthesized, and clean platform to investigate magnetic topological materials with marvellous quantum states [5–7], such as axion electrodynamics [5,8–10], the quantum Hall effect [4,11,12], and Majorana states [13]. Due to the limited available candidate materials, investigations on emergent phenomena in intrinsic magnetic topological materials are mostly focused on MnBi$_2$Te$_4$ [5,10,12,14,15]. Very recently, the Eu-based magnetic materials, including EuIn$_2$As$_2$, EuSn$_2$As$_2$, and EuSn$_2$P$_2$, have been demonstrated experimentally or proposed theoretically to be one family of the intrinsic magnetic topological materials [6,16–18].

EuSn$_2$P$_2$ crystallizes in a rhombohedral structure with the space group of $R\bar{3}m$ (No. 166) [Figs. 1(a) and 1(b)] [18], in analogy to the well-known topological insulator Bi$_2$Te$_3$. EuSn$_2$P$_2$ posses a two-dimensional (2D) crystal structure, in which each layer of trigonal Eu is sandwiched by two buckled

layers of honeycomb SnP [18]. Two adjacent layers of SnP are coupled by the van der Waals force. This kind of coupling makes EuSn$_2$P$_2$ being readily exfoliated to few-layer sheets for further detailed researches [6,7]. A previous investigation revealed that EuSn$_2$P$_2$ undergoes a paramagnetic (PM) phase to an A-type antiferromagnetic (AFM) phase transition around 30 K [18]. In the AFM state, magnetic moments of Eu^{2+} compose an A-type structure, i.e., ferromagnetic (FM) coupling in ab plane and antiferromagnetically coupled along the c axis. Furthermore, the recent investigations have revealed the appearance of long-range in-plane FM order triggering topological invariants and leading to the protection of Dirac states, as well as spin-momentum locking coexists with FM coupling in this material, promoting EuSn$_2$P$_2$ as an essential candidate axion insulator for topological antiferromagnetic spintronics applications [19]. Theorists have shown that if a material qualifies for an axion insulator, then critical behavior and a universal scaling can be established, which remains to be verified experimentally [20]. To acquire the modulation of the topological behaviors by magnetism, clarifying the magnetic interactions of EuSn$_2$P$_2$ is of prime importance. Particularly, the critical behavior of EuSn$_2$P$_2$, which could clear the nature of magnetic interactions, the spatial decay of correlation function, correlation length, and spin dimensionality at criticality [21–24], is still laking and deserves systematic investigations.

In this work, we performed a detailed investigation on the critical behavior as well as the anisotropic magnetic entropy change of the axion insulator candidate EuSn$_2$P$_2$ single crystals. The AFM ground state at $T_N = 30$ K is driven to a forced
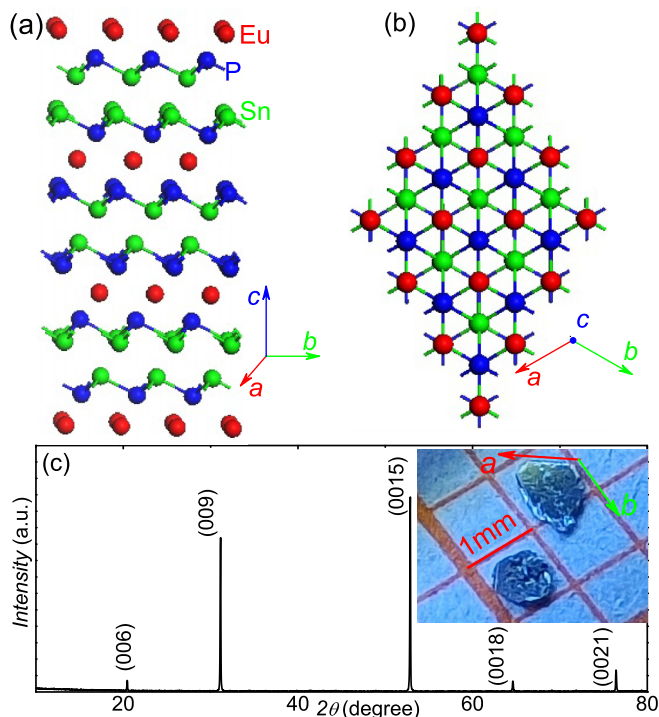
*xiaojunyang01@foxmail.com

FIG. 1. (a), (b) The crystal structure of $EuSn_2P_2$. (c) XRD patterns of $EuSn_2P_2$ single crystals. Inset: an optical photograph of $EuSn_2P_2$ single crystals.

FIG. 2. Left axis: Temperature-dependent zero-field-cooling (ZFC) magnetization at $H = 1$ kOe applied along $H//ab$ and $H//c$. Right axis: $1/(\chi - \chi_c)$ vs T at $H = 1$ kOe applied along two crystal orientations with linear fits by the Curie-Weiss law. Inset: Field-dependent magnetization $M(H)$ curves along two crystal orientations at $T = 2$ K.

ferromagnetic (FFM) state with an applied external magnetic field. The yielded Rhodes-Wolfarth ratio (RWR) is 1.13 (1.12) with $H//ab$ ($H//c$), confirming the FFM state in $EuSn_2P_2$ is weak itinerant. A large magnetocrystalline anisotropy constant $K_u = 521$ kJ/m^3 at 2 K is deduced. Furthermore, a set of self-consistent critical exponents is acquired, indicating a three-dimensional (3D) PM-FFM transition at 30 K. A $H - T$ phase diagram is constructed by a scaling analysis, where a field-induced tricritical point are determined. The values of $-\Delta S_M^{max}$ reaches 7.36 (6.41) J kg^{-1} K^{-1} with a field change of 50 kOe for $H//ab$ ($H//c$) near the PM-FFM phase transition, demonstrating that $EuSn_2P_2$ could be a candidate material for cryomagnetic refrigeration. The comprehensive study on the magnetic anisotropy, critical behaviors, and the magnetic interaction of the axion insulator candidate $EuSn_2P_2$ would prompt us in further comprehension of the unveiled nontrivial topological properties.

II. EXPERIMENTAL DETAILS

$EuSn_2P_2$ single crystals were fabricated by a Sn-flux method. The high-purity Eu ingots (99.97%), Sn shots (99.99%), and P powders (99.95%), all from Alfa Aesar, were mixed thoroughly, put into a crucible of corundum, and sealed into an evacuated quartz tube with the ratio of Eu : Sn : P = 1.1 : 20 : 2. The evacuated tube was heated to 1323 K at a rate of about 0.5 K/min, held for 10 h, and then cooled to 873 K at a rate of about 3 K/h. Then, the excess Sn is removed by centrifugation, and shiny hexagonal single crystals with typical sizes of $1 \times 1 \times 0.1$ mm^3 are harvested. Single-crystal x-ray diffraction (XRD) patterns, using a PANalytical x-ray

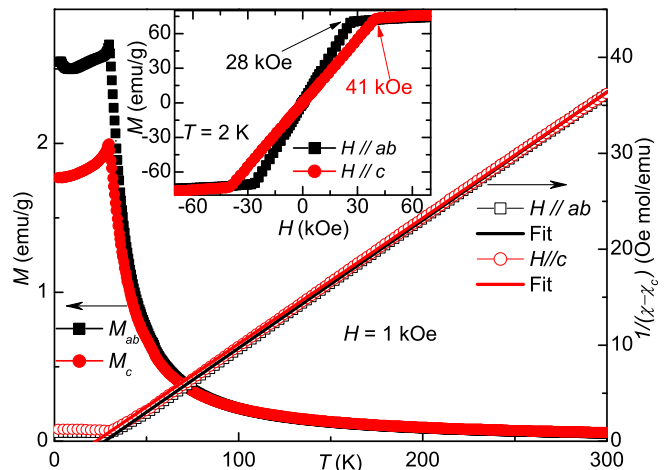diffractometer (Model EMPYREAN) with a monochromatic CuK$_{\alpha 1}$ radiation, were performed on the as grown sample, demonstrating the surface of the crystal is the $(0\ 0\ l)$ plane, as shown in Fig. 1(c). The interplane spacing is determined to be $c = 26.16$ Å, agreeing well with the previous reported value [18]. An optical photograph of $EuSn_2P_2$ single crystals with identified crystallographic axes are presented in inset of Fig. 1(c). Energy-dispersive x-ray (EDX) spectroscopy was collected by an Octane Plus Detector (AMETEX EDAX). The chemical composition determined by EDX is Eu:Sn:P = 1 : 2.03 : 1.96, with an error of about ¡À5% depending on the elements measured, which is consistent with the nominal composition with a nearly stoichiometric ratio. The magnetic properties were measured with a Quantum Design Evercool Magnetic Property Measurement System (MPMS XL-7).

III. RESULTS AND DISCUSSION

A. Magnetic properties

The temperature-dependent magnetization $M(T)$ at an applied field of 1 kOe from 2 to 300 K for $H//ab$ and $H//c$ is displayed in the left axis of Fig. 2, in which a transition to an AFM state is observed at around 30 K. Obviously, the magnetization at low temperature exhibits an anisotropic behavior, which is consistent with the 2D crystal structure in $EuSn_2P_2$. The magnetization at $H//ab$ is larger than $H//c$, indicating that the FM order is preferred within the ab plane rather than along the c axis [18]. The $M(T)$ curve exhibits an upturn below 8 K under $H//ab$, which is common behavior expected for an A-type antiferromagnet and the origin is still controversy [6,7,17,25]. The $M(T)$ curves of high temperature can be well characterized by the Curie-Weiss law [the right axis of Fig. 2], which gives the effective magnetic moment (μ_{eff}) of 7.74(1)/7.81(1) μ_B/f.u and the Weiss temperature of 27.3(1)/22.6(1) K for the in-plane ($H//ab$)/out-of-plane ($H//c$) field. The effective magnetic moments are compara-
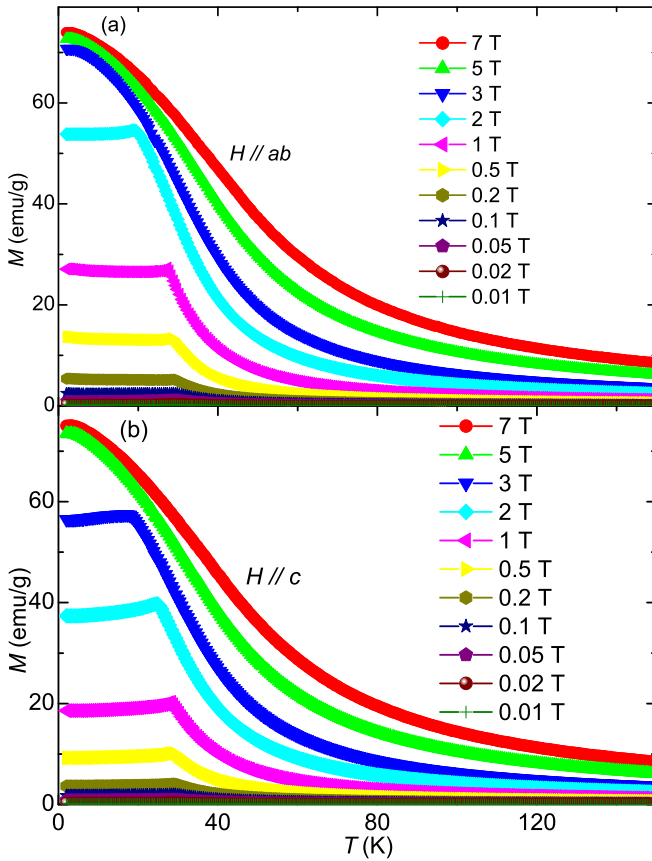
FIG. 3. Magnetization vs temperature curves under various fields along (a) $H//ab$, (b) $H//c$.

FIG. 4. The isothermal magnetization as a function of field $M(H)$ measured from $T = 2$ to 100 K under (a) $H//ab$, (b) $H//c$.

ble with the expected value of 7.94 μ_B for the ion of Eu^{2+} within the experimental error. The positive values of the Weiss temperature demonstrates that the FM interactions dominate in the PM state in $EuSn_2P_2$. The isothermal field-dependent magnetization $M(H)$ at $T = 2$ K is displayed in the inset of Fig. 2. At low fields, magnetization increases linearly with fields exhibiting typical behavior of an antiferromagnet. Upon increasing the field to $H_{ab} = 28$ kOe ($H_c = 41$ kOe), M leaps to plateaus, implying the presence of the forced ferromagnetic (FFM) phase. At $H = 70$ kOe the saturated magnetization μ_s reaches 6.01 and 6.16 μ_B/f.u. for $H//ab$ and $H//c$, respectively. The μ_s is smaller than the full 7.0 μ_B/f.u. expected for a localized Eu^{2+}, which could be due to the possible itinerant characterization of FM state in $EuSn_2P_2$ or our applied field of 70 kOe is not high enough [7]. The origin deserves further investigation. With the generated effective moments and saturated moments, the Rhodes-Wohlfarth ratio (RWR) can be evaluated. RWR is equal to P_c/P_s, where P_s equals the saturated moment (μ_s) and P_c is associated with the effective moment (μ_{eff}), i.e., $P_c(P_c + 2) = \mu_{eff}^2$ [26,27]. RWR should be equal to 1 for a localized FM material and becomes larger than 1 in an itinerant system. In our $EuSn_2P_2$ sample, RWR is calculated to be 1.13 and 1.12 with $H//ab$ and $H//c$, respectively, demonstrating an weak itinerant characterization.

The temperature-dependent magnetization measured under different fields is displayed in Figs. 3(a) and 3(b) for $H//ab$ and $H//c$, respectively. The behavior further indicates the
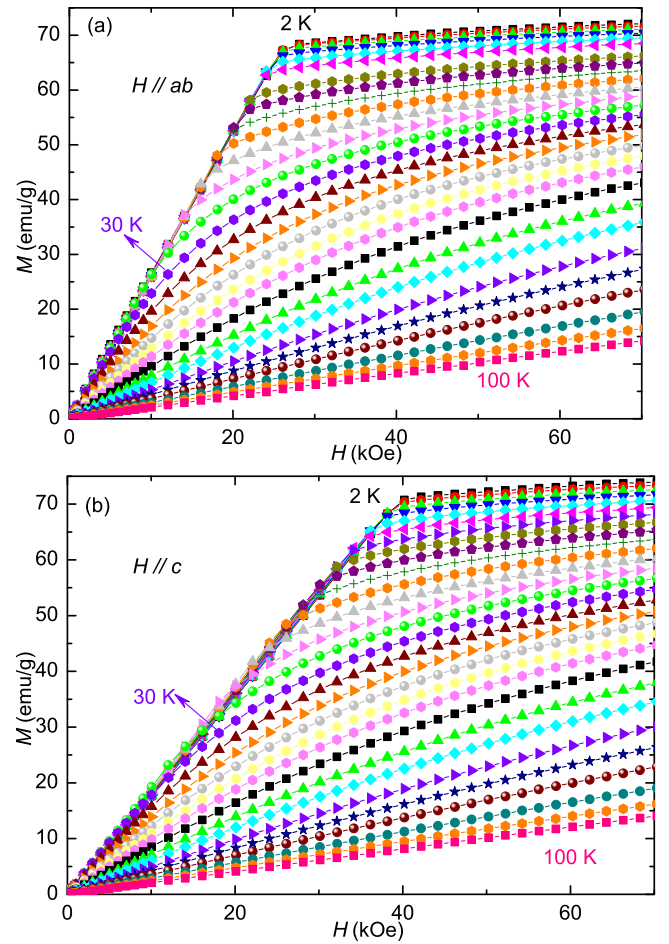
presence of the forced ferromagnetic (FFM) phase under high fields and could be explained as an A-type AFM order driven to FFM state by high magnetic fields [28]. Figures 4(a) and 4(b) display the magnetization as a function of field $M(H)$ from 2 to 100 K with fields up to 70 kOe applied along $H//ab$ and $H//c$, respectively. At high temperature, the plots of $M(H)$ exhibit a linear paramagnetic behavior. At low temperature, the $M(H)$ curves show linear increases under low applied fields and the magnetization is driven to a FFM state under high applied fields. Considering the following reasons, we argue the high field polarized state to be a FM state. First, previous investigations revealed the presence of long-range ferromagnetic order triggering topological invariants and clear evidence that layer-dependent spin-momentum locking coexists with ferromagnetism in $EuSn_2P_2$ [19]. Second, the following critical behavior and scaling analyses should be applicable in a system with a second-order ferromagnetic transition. Third, the following estimated magnetic specific heat change $\Delta C_p(T, H)$ exhibits typical features of a ferromagnet. Forth, as the universality principle for magnetic entropy change ($\Delta S_M(T, H)$) is only applicable in FM state, the well collapsed data of scaled $\Delta S_M(T, H)$ in high field confirms the presence of FFM state in high field region.

To learn more about the anisotropy in $EuSn_2P_2$, we evaluated the magnetocrystalline anisotropy constant K_u, which
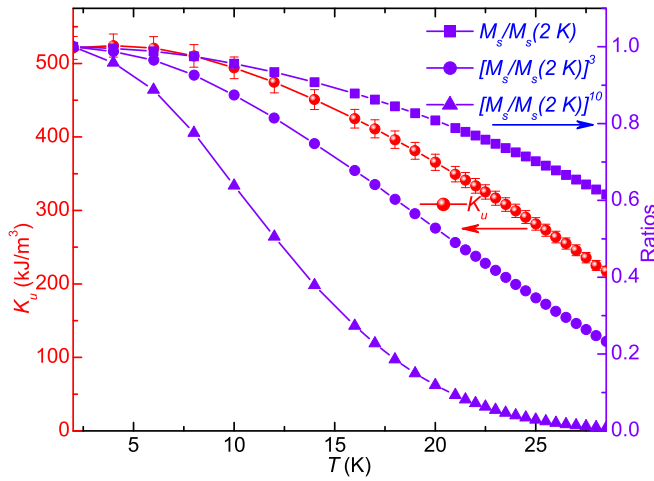
FIG. 5. Temperature-dependent (left axis) the anisotropy constant K_u and (right axis) the ratios of $[M_s/M_s(2K)]^{n(n+1)/2}$ with $n = 1$, 2, and 4.

can be estimated by the formula, $2K_u/M_s = \mu_0 H_s$, where, M_s is the in-plane saturation magnetization, μ_0 denotes the vacuum permeability, H_s reprents the field at which saturation magnetization occurs [29]. The calculated values of K_u versus temperature are depicted in the left axis of Fig. 5. The derived K_u gradually decreases with an increasing temperature, which is commonly found in FM systems and could arise from fluctuating of magnetic moments and be activated by a nonzero thermal energy [30,31]. The derived $K_u = 521$ kJ/m^3 at 2 K, which is relatively larger than that values of other 2D magnetic systems such as CrBr$_3$ ($\approx$86 kJ/m^3 at 5 K) [32], CrI$_3$ ($\approx$300 kJ/m^3 at 5 K) [32], Cr$_2$Si$_2$Te$_6$ ($\approx$65 kJ/m^3 at 2 K) [33], and Cr$_2$Ge$_2$Te$_6$ ($\approx$20 kJ/m^3 at 2 K) [33], suggesting the magnetocrystalline anisotropy in EuSn$_2$P$_2$ is strong and making it a promising material from the technological point of view. Based on a classical theory, $\langle K^n \rangle \propto M_s^{n(n+1)/2}$, where M_s represents the saturation magnetization and $\langle K^n \rangle$ is the expectation value of anisotropy for the nth power angular function, in the case of an uniaxial anisotropy $n = 2$ and a cubic anisotropy $n = 4$, leading to exponents of 3 and 10, respectively [30,31]. In the right axis of Fig. 5, temperature-dependent $[M_s/M_s(2K)]^{n(n+1)/2}$ with $n = 1$, 2, and 4 are presented, which indicates that the magnetocrystalline anisotropy in EuSn$_2$P$_2$ cannot be simply characterized by an uniaxial anisotropy or a cubic anisotropy, exhibiting a complicated magnetic structure.

B. Critical behavior

For a system with a second-order FM transition, the analysis on critical behavior could reveal the origin of the spatial decay of the correlation function, the correlation length, the magnetic interactions, and the spin dimensionality at criticality [21–24]. The spontaneous magnetization (M_s) versus field below T_C, the field-dependent magnetization (M) at T_C, and the initial magnetic susceptibility (χ_0^{-1}) versus temperature above T_C of a second-order FM transition can be characterized by several critical exponents β, δ, and γ, respectively [34,35].

The mathematical definition of the critical exponents are as follows:

$$M_s(T) \propto |\varepsilon|^\beta, \quad \varepsilon < 0, \quad \text{below } T_C, \tag{1}$$

$$M \propto H^{1/\delta}, \quad \varepsilon = 0, \quad T = T_C, \tag{2}$$

$$\chi_0^{-1}(T) \propto |\varepsilon|^\gamma, \quad \varepsilon > 0, \quad \text{above } T_C, \tag{3}$$

where $\varepsilon = T/T_C - 1$ represents the reduced temperature. On the basis of the Arrott plots (a mean-field model) with $\beta = 0.5$ and $\gamma = 1.0$, the plots of M^2 versus H/M should be consist of a set of linear parallel lines [36], in which the curve at T_C should go through the original point (0,0). The Arrott plots for EuSn$_2$P$_2$ are shown in Fig. 6(a). The nonlinear behavior demonstrates that the mean-field model is not a proper one to characterize the magnetism in EuSn$_2$P$_2$. According to a criterion by Banerjee [37], the phase transition of second (first) order suggests a positive (negative) slope. The slopes of the Arrott plots changed from negative in low-field region to positive in high-field region [inset of Fig. 6(a)], implying the field induced AFM-FFM transition is of a first order and temperature induced PM-FFM transition in high-field region is of a second order [38]. To better characterize the isothermals, we employ a modified Arrott plot with the Arrott-Noaks equation [39]:

$$(H/M)^{1/\gamma} = a\varepsilon + bM^{1/\beta}, \tag{4}$$

where a and b are constants. Figures 6(b)–6(f) display the modified Arrott plots using theoretical critical exponents of the 2D Ising model ($\beta = 0.125$, $\gamma = 1.75$), the 3D Heisenberg model ($\beta = 0.365$, $\gamma = 1.386$), the 3D Ising model ($\beta = 0.325$, $\gamma = 1.24$), the 3D XY model ($\beta = 0.345$, $\gamma = 1.316$), and the tricritical mean-field model ($\beta = 0.25$, $\gamma = 1.0$). For a perfect model, the modified Arrott plot should be consist of various parallel straight lines with slopes $S(T)$ equal $dM^{1/\beta}/d(H/M)^{1/\gamma}$. To discover the best model to describe the isothermals, we derive the normalized slope (NS), $S_N = S(T)/S(T_C)$ [Fig. 7(a)]. For an ideal model, the NS should be equal to 1. Clearly, the critical behavior of EuSn$_2$P$_2$ cannot be characterized by any universal classes of models. Thus, we employ an self-consistent iterative method to get a proper modified Arrott plot with suitable critical exponents [40–42]. The high-field region of the achieved modified Arrott plots are presented in Fig. 7(b).

From the modified Arrott plots, the M_s and χ_0^{-1} can be extrapolated [Fig. 8(a)]. Fitting the curves by Eqs. (1) and (3) generates $\beta = 0.281(1)$ with $T_C = 30.2(1)$ K and $\gamma = 0.77(3)$ with $T_C = 30.1(1)$ K. According to Eq. (3), a linear fits to the $M(H)$ curve at T_C in $\log_{10}$-$\log_{10}$ scale yields $\delta = 3.76(4)$ [inset of Fig. 8(a)]. The accuracy and self-consistency of the generated exponents can be checked by the Widom relation $\delta = 1 + \gamma/\beta$ [43]. Using the fitted values of β and γ, we calculate $\delta = 3.74(14)$, which matches well with the above fitted value of δ, demonstrating that the above critical-behavior analysis is self-consistent. Critical exponents of β and γ can also be acquired by the Kouvel-Fisher (KF) relation [44], $M_s(T)/(dM_s(T)/dT) = (T - T_C)/\beta$ and $\chi_0^{-1}(T)/(d\chi_0^{-1}(T)/dT) = (T - T_C)/\gamma$. Linear fits to the plots of $M_s(T)/(dM_s(T)/dT)$ and $\chi_0^{-1}(T)/(d\chi_0^{-1}(T)/dT)$ as
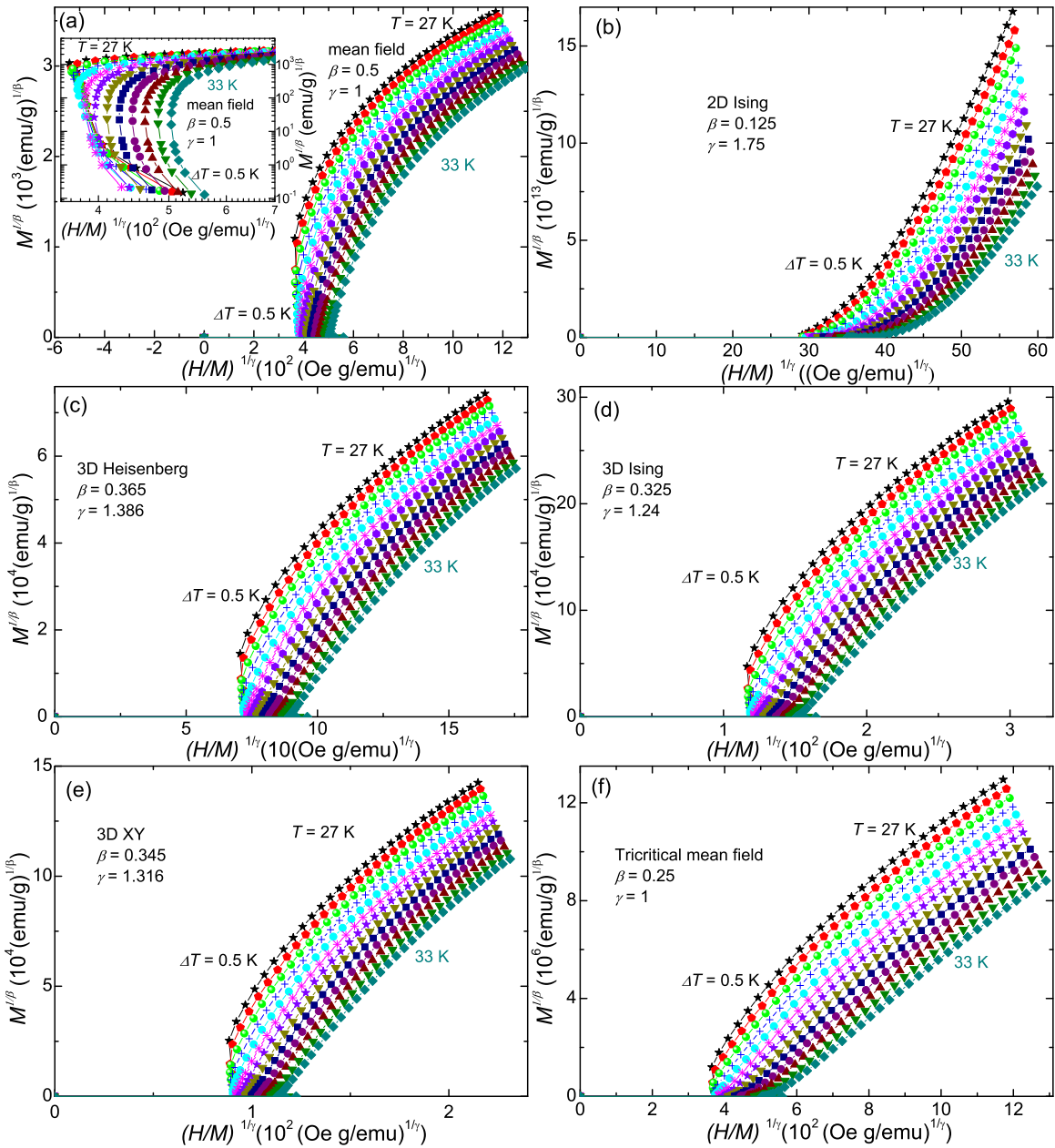
FIG. 6. The modified Arrott plots of $M^{1/\beta}$ vs $(H/M)^{1/\gamma}$ for $H//ab$ with parameters of a (a) mean-field model, (b) 2D Ising model, (c) 3D Heisenberg model, (d) 3D Ising model, (e) 3D XY model, and (f) tricritical mean-field model. Inset of (a) the Arrott plots in a $\log_{10}$-$\log_{10}$ scale.

a function of temperature generate $\beta = 0.281(8)$ with $T_C = 30.1(4)$ K and $\gamma = 0.74(2)$ with $T_C = 30.2(6)$ K [Fig. 8(b)].

Scaling analyses can be utilized to further examine the accuracy of the generated exponents. In the asymptotic critical region, the scaling relation can be expressed as [43]

$$M(H, \varepsilon) = \varepsilon^{\beta} f_{\pm}(H/\varepsilon^{\beta+\gamma}), \qquad (5)$$

where f_+ for $T > T_C$ and f_- for $T < T_C$ represent regular functions. The above scaling equation can be reduced to $m = f_{\pm}(h)$ by defining rescaled magnetization $m = M|\varepsilon|^{-\beta}$ and rescaled field $h = H|\varepsilon|^{-(\beta+\gamma)}$. It suggests that the scaled m versus h will collapse onto two separate universal curves with properly derived critical exponents. Figure 9 displays plots of the scaled m versus the scaled h in high-field region with a $\log_{10}$-$\log_{10}$ scale, in which all curves fall into two branches

below T_C and above T_C. Moreover, the scaling equation can also take another form [34],

$$\frac{M}{H^{\delta}} = g\left(\frac{\varepsilon}{H^{1/\beta}}\right), \qquad (6)$$

where $g(x)$ represents a regular scaling function. According to Eq. (6), with suitable exponents all the curves should fall into a single universal one. This is indeed observed in the inset of 9, i.e., plots of $MH^{-1/\delta}$ versus $\varepsilon H^{-1/(\beta\delta)}$ in high-field region collapse onto a universal curve. The above scaling analyses further demonstrate the generated critical exponents are accurate and reliable.

The we discuss the scaling in low-field region. Above T_C, the experimental data in low-field region collapse also well in m versus h scaling curves. However, below T_C, the low-
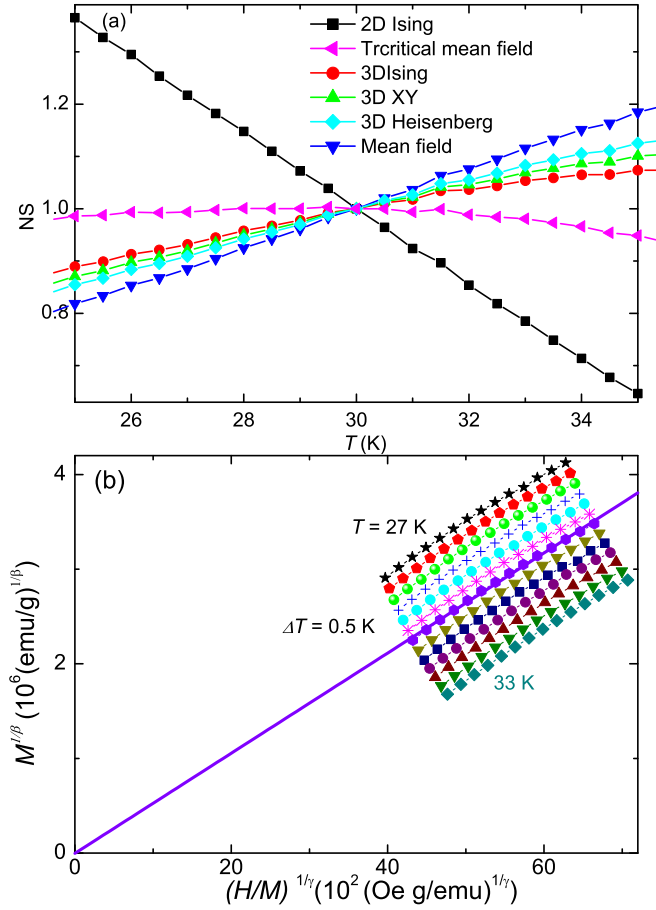
FIG. 7. (a) Temperature-dependent normalized slopes (NS) $S_N = S(T)/S(T_C)$ for different theoretical universal models. (b) $M^{1/\beta}$ vs $(H/M)^{1/\gamma}$ curves (the modified Arrott plots) with $\beta = 0.281$ and $\gamma = 0.77$.
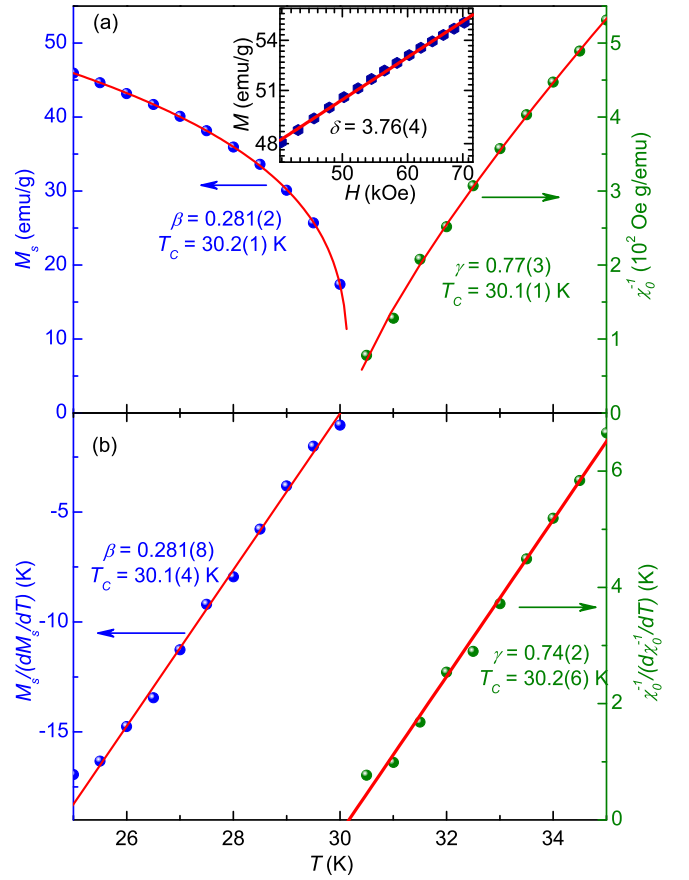

FIG. 8. (a) Temperature-dependent (left) the spontaneous magnetization M_s and (right) the inverse initial susceptibility $1/\chi_0$ with solid fits based on Eqs. (1) and (3) for EuSn$_2$P$_2$. Inset: M vs H on a $\log_{10}$- $\log_{10}$ scale at $T_C = 30$ K with a linear fitting. (b) (Left) $M_s(dM_s/dT)^{-1}$ and (right) $\chi_0^{-1}(d\chi_0^{-1}/dT)^{-1}$ vs temperature (the Kouvel-Fisher plot) with linear fits.

field experimental data cannot collapse onto one universal curve due to the presence of AFM phase, as displayed in Fig. 10, in which the boundary between the AFM and the FFM states can be determined. The inset of Fig. 10 displays the H-T phase diagram of EuSn$_2$P$_2$ single crystal with $H//ab$, where a tricritical point on the boundaries of the paramag-

netic, antiferromagnetic, and forced ferromagnetic states can be determined at temperature and field of (30 K, 16.7 kOe).

The deduced critical exponents of EuSn$_2$P$_2$ and theoretically predicted exponents for different universal models are summarized in Table I. The exponent β of 2D magnets should be within a window of $0.1 \leqslant \beta \leqslant 0.25$ [46]. The obtained

TABLE I. Comparison of the deduced exponents of EuSn$_2$P$_2$ with different universal models. (MAP = the modified Arrott plot, KFP = the Kouvel-Fisher plot, CI = the critical isotherm, and cal = calculated.

| Composition	Technique	Ref.	β	γ	δ	n	m
EuSn$_2$P$_2$	MAP	This work	0.281(2)	0.77(3)	3.74(14)$^{\text{cal}}$		
	KFP	This work	0.281(8)	0.74(2)	3.63(14)$^{\text{cal}}$		
	CI	This work			3.76(4)		
	ΔS_M^{max}	This work				0.768(7)	
	RCP	This work					1.531(14)
Mean field	Theory	[36]	0.5	1.0	3.0	0.667	1.333
3D Heisenberg	Theory	[36]	0.365	1.386	4.8	0.637	1.208
Tricritical mean field	Theory	[37]	0.25	1.0	5	0.4	1.20
2D Ising	Theory	[45]	0.125	1.75	15	0.533	1.06
3D XY	Theory	[36]	0.345	1.316	4.81	0.606	1.208
3D Ising	Theory	[36]	0.325	1.24	4.82	0.569	1.207
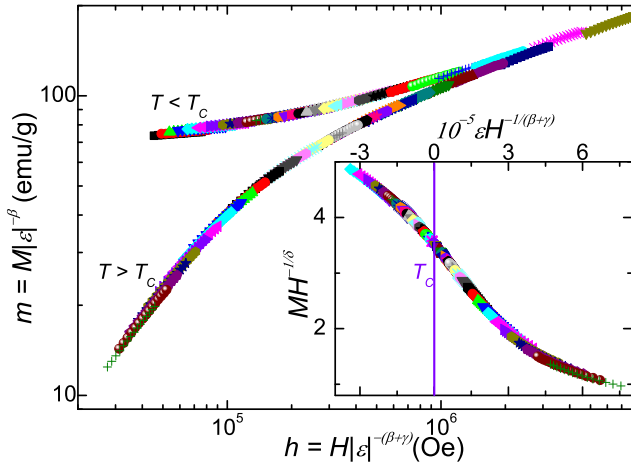
FIG. 9. Scaling plots of $m = M|\varepsilon|^{-\beta}$ vs $h = H|\varepsilon|^{-(\beta+\gamma)}$ on a $\log_{10}$-$\log_{10}$ scale in high field region. Inset: $MH^{-1/\delta}$ vs $\varepsilon H^{-1/(\beta\delta)}$ curves.

value of β demonstrates a 3D critical behavior in EuSn$_2$P$_2$. For the existing theoretical universal models, the tricritical mean-field model best describes the deduced critical exponents, but there are still relatively large deviations.

Then, we make a discussion on the nature as well as the range of interactions in EuSn$_2$P$_2$. According to the renormalization-group theory [47,48], the interaction decays with distance r as $J(r) \sim r^{-(d+\sigma)}$, where d denotes the spatial dimensionality, and σ related to the range of the interaction. Moreover, the exponent γ follows the relation

$$\gamma = 1 + \frac{4}{d}\frac{(n+2)}{(n+8)}\Delta\sigma$$

$$+ \frac{8(n+2)(n-4)}{d^2(n+8)^2} \times \left[1 + \frac{2G(\frac{d}{2})(7n+20)}{(n-4)(n+8)}\right]\Delta\sigma^2, \quad (7)$$

where $\Delta\sigma = \sigma - d/2$, $G(\frac{d}{2}) = 3 - \frac{1}{4}(\frac{d}{2})^2$, and n represents the spin dimensionality. When $\sigma > 2$, a short-range magnetic interaction is valid, and $J(r)$ decays faster than r^{-5}.
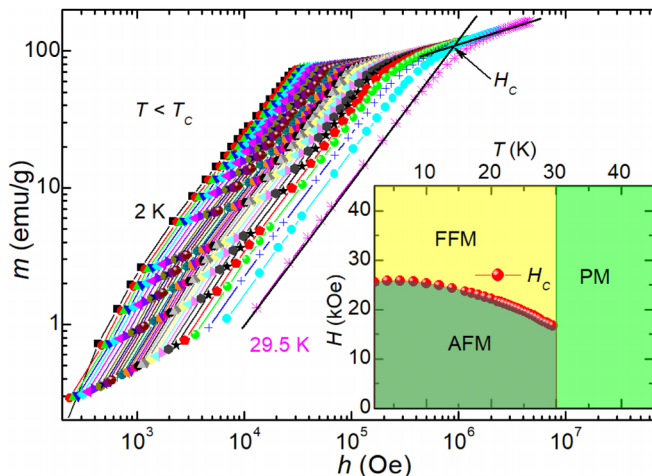

FIG. 10. m vs h/m below T_C on a $\log_{10}$-$\log_{10}$ scale. Inset: The $H - T$ phase diagram of EuSn$_2$P$_2$ with $H//ab$.

When $\sigma \leqslant 3/2$, a long-range magnetic interaction takes effect, where $J(r)$ decays slower than $r^{-4.5}$. In the case of EuSn$_2$P$_2$, σ can be estimated to less than 1.02, indicating a long-range magnetic interaction with the exchange interaction decays slower than $r^{-4.02}$.

C. Magnetic entropy change

Based on the classical thermodynamical theory and the Maxwell thermodynamic relations, the magnetic entropy change [$\Delta S_M(T, H)$] can be expressed as [49,50]

$$\Delta S_M(T, H) = \int_0^H \left(\frac{\partial M}{\partial T}\right)_H dH. \quad (8)$$

On the basis of Eq. (8), we calculated the magnetic entropy change under various fields with $H//ab$ and $H//c$ as presented in Figs. 11(a) and 11(b), respectively. Each $\Delta S_M(T)$ curve exhibits a peak around $T \sim 30$ K, indicating that the magnetic entropy change gets the maximum at the phase transition temperature. The maximum value of the $-\Delta S_M^{\max}$ reaches 9.47 (8.67) J kg^{-1} K^{-1} at $H = 70$ kOe and 7.36 (6.41) J kg^{-1} K^{-1} at $H = 50$ kOe for the $H//ab$ ($H//c$). The $-\Delta S_M^{\max}$ of EuSn$_2$P$_2$, is smaller than that of well-known magnetic refrigerating materials with a first-order FM phase transition, such as, 19 J kg^{-1} K^{-1} in Gd$_5$Si$_2$Ge$_2$ at 50 kOe [51], is larger than that of common low-dimensional systems at second-order FM phase transitions, such as, 3 J kg^{-1} K^{-1} in VI$_3$ [52], 2.2 J kg^{-1} K^{-1} in CrSbSe$_3$ [53], and 3.2 J kg^{-1} K^{-1} in PrCrGe$_3$ at 50 kOe [41], and is comparable with that of well-known materials suitable for magnetic refrigerating with second-order FM transitions, for example, 7.0 J kg^{-1} K^{-1} in CdCr$_2$S$_4$ and 6.9, 5.2, and 7.0 J kg^{-1} K^{-1} in Ln$_6$Co$_{1.67}$Si$_3$ (Ln = Pr, Gd, and Tb) at 50 kOe [54,55]. Moreover, it is worth noting that the magnetic entropy change of systems with second-order FM transitions is reversible, which is preferred for practical use, making EuSn$_2$P$_2$ a candidate material for low-temperature magnetic refrigeration.

Then, we concentrate on the anisotropy of the magnetic entropy change. Under $H//c$, negative values of $\Delta S_M(T, H)$ are detected at $H = 20$ kOe and 30 kOe at temperatures below T_C; however, under $H//ab$, all the values of that are positive at $H = 20$ kOe and 30 kOe, revealing a large anisotropy in EuSn$_2$P$_2$. The presence of negative values of $\Delta S_M(T, H)$ could be due to the competition of the magnetization and the magnetic anisotropy [41,52,56]. To learn more about the magnetic anisotropy, the rotating magnetic entropy change $\Delta S_M^R(T, H) = \Delta S_M(T, H_{ab}) - \Delta S_M(T, H_c)$, is evaluated and displayed in Fig. 11(c), which reaches a maximum of 1.38 J kg^{-1} K^{-1} around T_C, further exhibiting the anisotropic feature.

Exploiting the acquired $\Delta S_M(T, H)$, we can calculate the magnetic specific heat change [57], $\Delta C_p(T, H) = T\frac{\partial \Delta S_M(T, H)}{\partial T}$, which exhibiting typical behaviors of a ferromagnet, i.e., the curves of $\Delta C_p(T, H)$ change from negative in ferromagnetic phase to positive in the paramagnetic one with an increasing of temperature and all the plots of $\Delta C_p(T)$ curves pass through the zero point at T_C [Figs. 12(a) and 12(b)]. $T_C \sim 29.9(3)$ K and 29.8(4) K can be determined at $\Delta C_p(T) = 0$ for $H//ab$ and $H//c$, respectively, which is compatible with the value obtained by critical-behavior analysis.
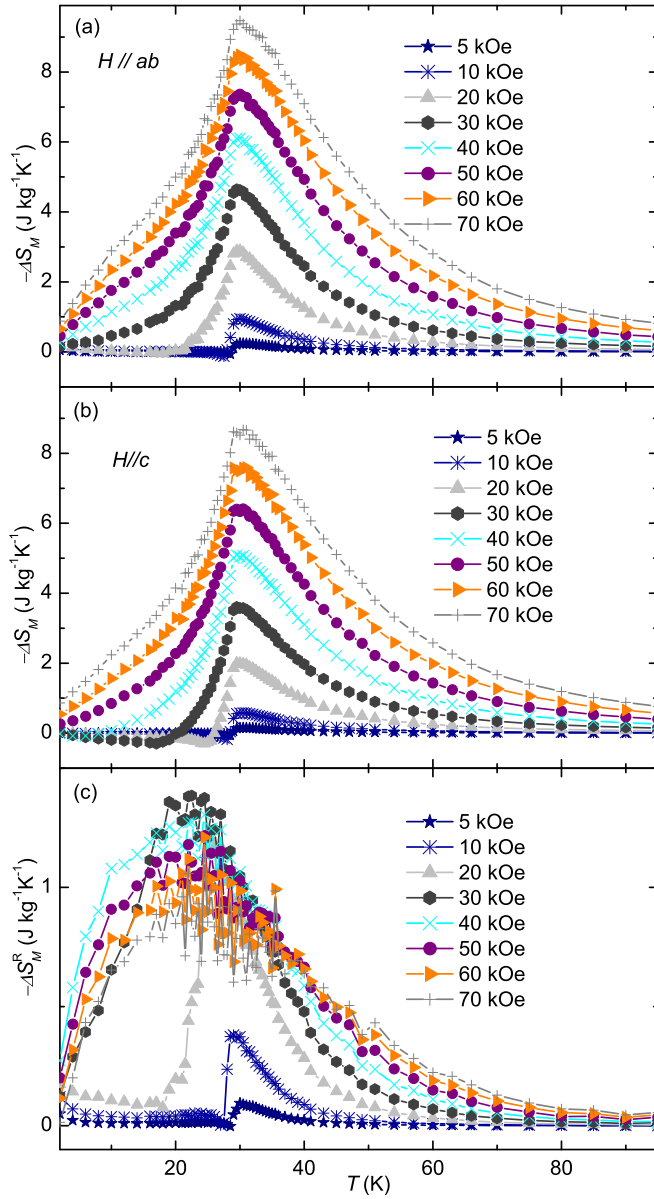
FIG. 11. (a), (b) The magnetic entropy change $[\Delta S_M(T, H)]$ as a function of temperature of $EuSn_2P_2$ for different fields along (a) $H//ab$ and (b) $H//c$. (c) Rotating magnetic entropy change $[\Delta S_M^R(T, H) = \Delta S_M(T, H_ab) - \Delta S_M(T, H_c)]$ vs T under various fields for $EuSn_2P_2$.

As the field increases to the FFM region, parameters of $\Delta S_M(T, H)$ curve follow a series of power laws [58–60]:

$$-\Delta S_M^{\max} \propto H^n, \quad RCP \propto H^m, \quad (9)$$

where $-\Delta S_M^{\max}$ represents the maximum of the $-\Delta S_M$, RCP denotes the relative cooling power $RCP = -\Delta S_M^{\max} \times \delta_{\mathrm{FWHM}}$ (δ_{FWHM} is the full width at half maximum of $-\Delta S_M$), and n and m are associated with the critical exponents (β, γ, and δ) as follows [59,60]:

$$n(T_C) = 1 + (\beta - 1)/(\beta + \gamma), \quad (10)$$
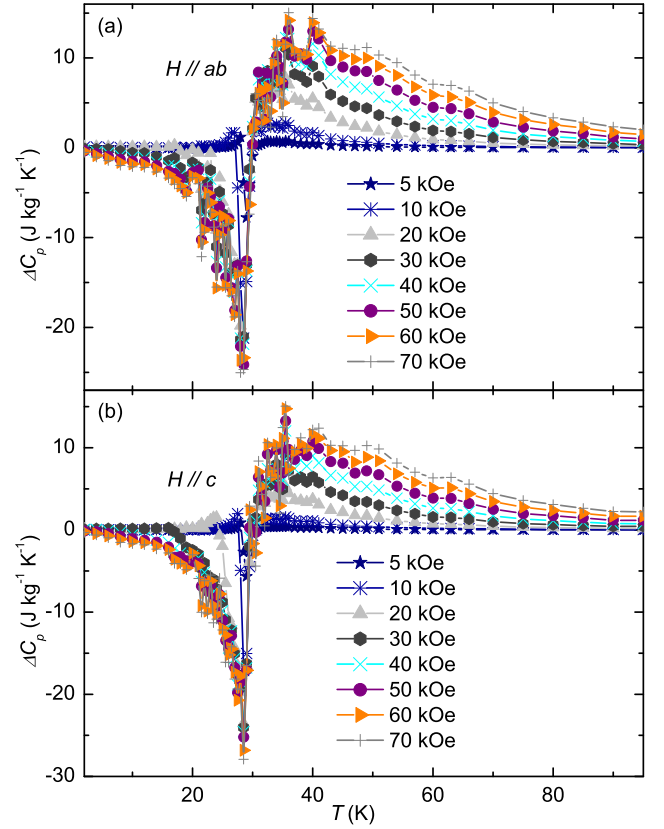
$$m = 1 + 1/\delta. \quad (11)$$

FIG. 12. (a), (b) The magnetic specific heat change $[\Delta C_p(T, H)]$ as a function of temperature of $EuSn_2P_2$ for different fields along (a) $H//ab$ and (b) $H//c$.

The field dependence of $-\Delta S_M^{\max}$ and RCP under $H//ab$ are displayed in the left and right axis of Fig. 13, respectively. In the FFM region ($H > 40$ kOe), the $-\Delta S_M^{\max}$ and RCP can be well fitted by Eqs. (10) and (11), yielding $n = 0.768(7)$ and $m = 1.531(14)$, respectively. The deviation from power law at low-field region is consistent with the existence of the AFM state, and only under high field the FFM state dominates, in which the power law takes effect.
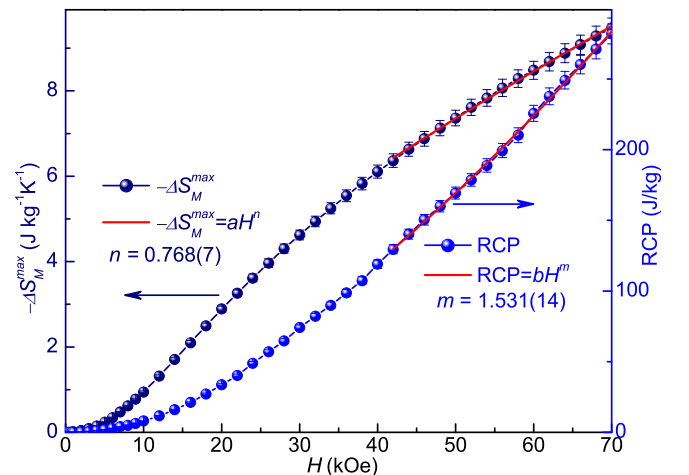

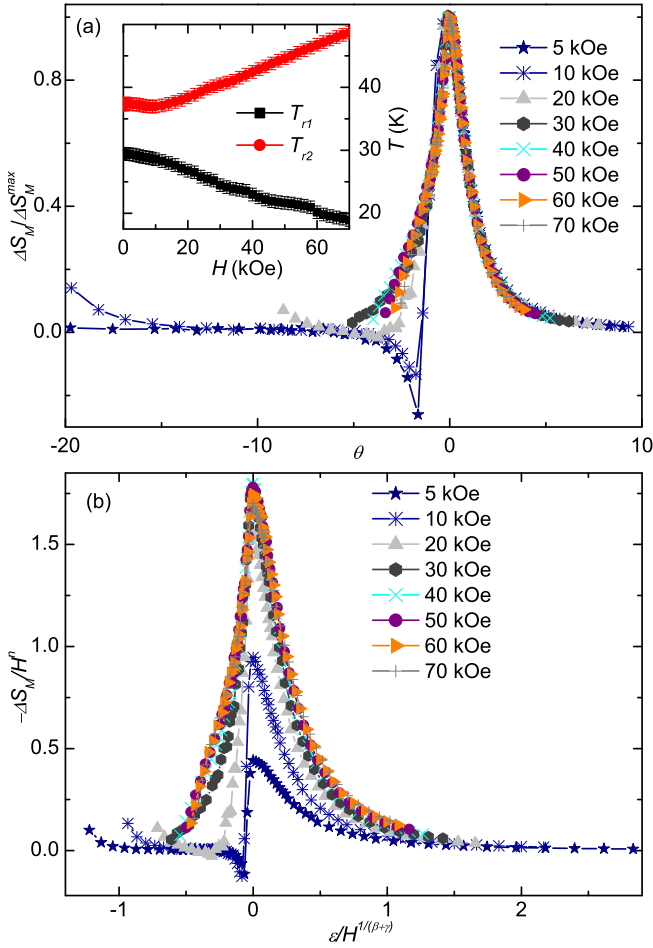FIG. 13. Field-dependent $\Delta S_M^{\max}$ and RCP for $H//ab$.

FIG. 14. (a) The normalized magnetic entropy change $\Delta S_M / \Delta S_M^{\max}$ vs the reduced temperature t curves. Inset: Field-dependent T_{r1} and T_{r2}. (b) $\Delta S_M(T, H)$ scaled by the deduced exponents.

On the basis of the universality principle, in the FM region $-\Delta S_M(T, H)$ can be normalized into a universal curve [60], i.e., $-\Delta S_M(T, H)$ can be scaled as $\Delta S'_M = \Delta S_M / \Delta S_M^{\max}$, and the temperature is renormalized into a scaled temperature θ defined as [61]

$$\theta_- = (T_C - T)/(T_{r1} - T_C), \text{ below } T_C, \quad (12)$$

$$\theta_+ = (T - T_C)/(T_{r2} - T_C), \text{ above } T_C, \quad (13)$$

where T_{r1} and T_{r2} [the inset of Fig. 14(a)], corresponding to $\Delta S_M(T_{r1}, T_{r2}) = \frac{1}{2} \Delta S_M^{\max}$, represent reference temperatures below and above T_C, respectively. As displayed in Fig. 14(a), all curves collapse into a universal curve under high fields in the FFM region, confirming the high-field PM-FFM transition is of a second order. Furthermore, the $\Delta S_M(T, H)$ can also be reorganized by another scaled equation,

$$-\Delta S_M \propto H^n F\left(\frac{\varepsilon}{H^{1/(\beta+\gamma)}}\right), \quad (14)$$

where β, γ, and n represent the critical exponents and $F(x)$ denotes a regular scaling function [62]. Figure 14(b) gives

$\frac{-\Delta S_M(T)}{H^n}$ versus $\frac{\varepsilon}{H^{1/(\beta+\gamma)}}$, where all the plots collapse onto a universal curve under high fields in the FFM region, confirming the validity and reliability of the obtained exponents. As the universality principle is only applicable in FM state, the well collapsed data in high field confirms the presence of FFM state in high field region, and the divergence in low-field region is consistent with the AFM state in low field.

Recent investigations have indicated that the magnetic interaction and/or magnetic structure are of prime importance to the formation and modulation of nontrivial topological states [63,64]. In MnSi, studies on the critical behavior as well as polarized neutron scattering prompt the suggestion of the existence a nontrivial skyrmion phase [65,66]. In PrAlGe, the FM ordering induces the band splitting and leads to the shift of Weyl nodes to break time-reversal symmetry [63,67]. In NdSb, the AFM ground state is a Dirac semimetal while the FFM state becomes a Weyl semimetal [68,69]. Detailed scaling analysis and establishment of the phase diagram, which clearly characterizes the relationships between magnetic field, temperature and magnetic order in $EuSn_2P_2$, is influential for understanding the topological nature of $EuSn_2P_2$. The recent investigations have presented that spin momentum locking coexists with FM coupling in $EuSn_2P_2$ [19], pointing it meets the hallmarks to be an axion insulator. Moreover, it have been shown that if a material system qualifies for axion insulating behavior, critical behavior and a universal scaling can be established [20]. The well-established scaling behavior of the magnetization and the magnetic entropy change further supports $EuSn_2P_2$ to be an axion insulator.

IV. CONCLUSIONS

In summary, we have performed a detailed investigation on the anistropic magnetic properties of the axion insulator candidate $EuSn_2P_2$ single crystal. As the field increases, the AFM transition at $T \sim 30$ K is driven to a FFM phase. The acquired RWR reveals the ferromagnetism is weak itinerant. The exponents β, δ, and γ deduced from several techniques matches well and follows scaling equations, indicating the estimated critical exponents are reliable and intrinsic. The exponents exhibit a 3D critical behavior. The large $-\Delta S_M(T, H)$ and RCP indicates that $EuSn_2P_2$ could be a promising candidate material for cryomagnetic refrigeration. A tricritical point at temperature and field of (30 K, 16.7 kOe) is determined. Our work reveals valuable information on magnetic properties for future investigation and application.

[1] M. Z. Hasan and C. L. Kane, Rev. Mod. Phys. **82**, 3045 (2010).

[2] M. He, H. Sun, and Q. L. He, Front. Phys. **14**, 43401 (2019).

[3] W. Bi, T. Culverhouse, Z. Nix, W. Xie, H. J. Tien, T. R. Chang, U. Dutta, J. Zhao, B. Lavina, E. E. Alp, D. Zhang, J. Xu, Y. Xiao, and Y. K. Vohra, npj Quantum Mater. **7**, 43 (2022).

[4] R. Yu, W. Zhang, H. J. Zhang, S. C. Zhang, X. Dai, and Zhong Fang, Science **329**, 61 (2010).

[5] D. Q. Zhang, M. J. Shi, T. S. Zhu, D. Y. Xing, H. J. Zhang, and J. Wang, Phys. Rev. Lett. **122**, 206401 (2019).

[6] H. Li, S. Y. Gao, S. F. Duan, Y. F. Xu, K. J. Zhu, S. J. Tian, J. C. Gao, W. H. Fan, Z. C. Rao, J. R. Huang, J. J. Li, D. Y. Yan, Z. T. Liu, W. L. Liu, Y. B. Huang, Y. L. Li, Y. Liu, G. B. Zhang, P. Zhang, T. Kondo et al., Phys. Rev. X **9**, 041039 (2019).

[7] H. Li, W. Gao, Z. Chen, W. Chu, Y. Nie, S. Ma, Y. Han, M. Wu, T. Li, Q. Niu, W. Ning, X. Zhu, and M. Tian, Phys. Rev. B **104**, 054435 (2021).

[8] R. S. K. Mong, A. M. Essin, and J. E. Moore, Phys. Rev. B **81**, 245209 (2010).

[9] R. Li, J. Wang, X.-L. Qi, and S.-C. Zhang, Nat. Phys. **6**, 284 (2010).

[10] M. M. Otrokov, I. I. Klimovskikh, H. Bentmann, D. Estyunin, A. Zeugner, Z. S. Aliev, S. Gaß, A. U. B. Wolter, A. V. Koroleva, A. M. Shikin, M. Blanco-Rey, M. Hoffmann, I. P. Rusinov, A. Yu. Vyazovskaya, S. V. Eremeev, Yu. M. Koroteev, V. M. Kuznetsov, F. Freyse, J. Sánchez-Barriga, I. R. Amiraslanov et al., Nature (London) **576**, 416 (2019).

[11] H. Masuda, H. Sakai, M. Tokunaga, Y. Yamasaki, A. Miyake, J. Shiogai, S. Nakamura, S. Awaji, A. Tsukazaki, H. Nakao, Y. Murakami, T. H. T.-h. Arima, Y. Tokura, and S. Ishiwata, Sci. Adv. **2**, e1501117 (2016).

[12] Y. Deng, Y. Yu, M. Z. Shi, Z. Guo, Z. Xu, J. Wang, X. H. Chen, and Y. Zhang, Science **367**, 895 (2020).

[13] X.-L. Qi, T. L. Hughes, and S.-C. Zhang, Phys. Rev. B **82**, 184516 (2010).

[14] J. Li, Y. Li, S. Du, Z. Wang, B. L. Gu, S. C. Zhang, K. He, W. Duan1, and Y. Xu, Sci. Adv. **5**, eaaw5685 (2019).

[15] B. Chen, F. Fei, D. Zhang, B. Zhang, W. Liu, S. Zhang, P. Wang, B. Wei, Y. Zhang, Z. Zuo, J. Guo, Q. Liu, Z. Wang, X. Wu, J. Zong, X. Xie, W. Chen, Z. Sun, S. Wang, Y. Zhang et al. Nat. Commun. **10**, 4469 (2019).

[16] Y. F. Xu, Z. D. Song, Z. J. Wang, H. M. Weng, and X. Dai, Phys. Rev. Lett. **122**, 256402 (2019).

[17] Y. Zhang, K. Deng, X. Zhang, M. Wang, Y. Wang, C. Liu, J.-W. Mei, S. Kumar, E. F. Schwier, K. Shimada, C. Chen, and B. Shen, Phys. Rev. B **101**, 205126 (2020).

[18] X. Gui, I. Pletikosic, H. Cao, H. J. Tien, X. Xu, R. Zhong, G. Wang, T. R. Chang, S. Jia, T. Valla, W. Xie, and R. J. Cava, ACS Cent. Sci. **5**, 900 (2019).

[19] G. M. Pierantozzi, A. D. Vita, C. Bigi, X. Gui, H. J. Tien, D. Mondal, F. Mazzola, J. Fujii, I. Vobornik, G. Vinai, A. Sala, C. Africh, T. L. Lee, G. Rossi, T. R. Chang, W. Xie, R. J. Cava, and G. Panaccione, Proc. Natl. Acad. Sci. USA **119**, e2116575119 (2022).

[20] H. Li, H. Jiang, C.-Z. Chen, and X. C. Xie, Phys. Rev. Lett. **126**, 156601 (2021).

[21] M. E. Fisher, Rev. Mod. Phys. **46**, 597 (1974).

[22] H. E. Stanley, Rev. Mod. Phys. **71**, S358 (1999).

[23] Y. Liu, Z. Hu, E. Stavitski, K. Attenkofer, and C. Petrovic, Phys. Rev. B **103**, 144432 (2021).

[24] Y. Liu, Z. Hu, E. Stavitski, K. Attenkofer, and C. Petrovic, Phys. Rev. Res. **3**, 023181 (2021).

[25] J. Blawat, M. Marshall, J. Singleton, E. Feng, H. Cao, W. Xie, and R. Jin, Adv. Quantum Technol. **5**, 2200012 (2022).

[26] E. P. Wohlfarth, J. Magn. Magn. Mater. **7**, 113 (1978).

[27] T. Moriya, J. Magn. Magn. Mater. **14**, 1 (1979).

[28] Y. Liu and C. Petrovic, Phys. Rev. B **102**, 014424 (2020).

[29] B. D. Cullity and C. D. Graham, Introduction to Magnetic Materials (Wiley, Hoboken, NJ, 2009).

[30] C. Zener, Phys. Rev. **96**, 1335 (1954).

[31] W. J. Carr Jr., J. Appl. Phys. **29**, 436 (1958).

[32] N. Richter, D. Weber, F. Martin, N. Singh, U. Schwingenschlögl, B. V. Lotsch, and M. Kläui, Phys. Rev. Mater. **2**, 024004 (2018).

[33] Y. Liu and C. Petrovic, Phys. Rev. Mater. **3**, 014001 (2019).

[34] H. E. Stanley, Introduction to Phase Transitions and Critical Phenomena (Oxford University Press, London, UK, 1971).

[35] M. E. Fisher, Rep. Prog. Phys. **30**, 615 (1967).

[36] A. Arrott, Phys. Rev. **108**, 1394 (1957).

[37] S. K. Banerjee, Phys. Lett. **12**, 16 (1964).

[38] H. Han, W. Liu, Y. Dai, Y. Gao, Z. Tian, J. Fan, S. Zhou, L. Pi, C. Zhang, L. Zhang, and Y. Zhang, Phys. Rev. B **98**, 054403 (2018).

[39] A. Arrott and J. Noakes, Phys. Rev. Lett. **19**, 786 (1967).

[40] A. K. Pramanik and A. Banerjee, Phys. Rev. B **79**, 214426 (2009).

[41] X. Yang, J. Pan, S. Liu, M. Yang, L. Cao, D. Chu, and K. Sun, Phys. Rev. B **103**, 104405 (2021).

[42] X. Yang, J. Pan, K. Sun, Y. Shi, L. Cao, S. Liu, W. Gai, D. Chu, and M. Yang, J. Alloys Compd. **886**, 161118 (2021).

[43] B. Widom, J. Chem. Phys. **43**, 3898 (1965).

[44] J. S. Kouvel and M. E. Fisher, Phys. Rev. **136**, A1626 (1964).

[45] J. C. LeGuillou and J. Zinn-Justin, Phys. Rev. B **21**, 3976 (1980).

[46] A. Taroni, S. T. Bramwell, and P. C. Holdsworth, J. Phys.: Condens. Matter **20**, 275233 (2008).

[47] S. F. Fischer, S. N. Kaul, and H. Kronmuller, Phys. Rev. B **65**, 064443 (2002).

[48] M. E. Fisher, S. Ma, and B. G. Nickel, Phys. Rev. Lett. **29**, 917 (1972).

[49] V. K. Pecharsky and K. A. Gschneidner Jr., J. Magn. Magn. Mater. **200**, 44 (1999).

[50] D. Griffiths, Introduction to Electrodynamics, 3rd ed. (Prentice Hall, Englewood Cliffs, NJ, 1999), pp. 559–562.

[51] V. K. Pecharsky and K. A. Gschneidner, Jr., Phys. Rev. Lett. **78**, 4494 (1997).

[52] J. Yan, X. Luo, F. C. Chen, J. J. Gao, Z. Z. Jiang, G. C. Zhao, Y. Sun, H. Y. Lv, S. J. Tian, Q. W. Yin, H. C. Lei, W. J. Lu, P. Tong, W. H. Song, X. B. Zhu, and Y. P. Sun, Phys. Rev. B **100**, 094402 (2019).

[53] Y. Sun, Z. Song, Q. Tang, and X. Luo, J. Phys. Chem. C **124**, 11110 (2020).

[54] B. G. Shen, J. R. Sun, F. X. Hu, H. W. Zhang, and Z. H. Cheng, Adv. Mater. **21**, 4545 (2009).

[55] A. M. Tishin and Y. I. Spichkin, The Magnetocaloric Effect and Its Applications (Institute of Physics Publishing, Bristol, UK, 2003).

[56] G. T. Lin, X. Luo, F. C. Chen, J. Yan, J. J. Gao, Y. Sun, W. Tong, P. Tong, W. J. Lu, Z. G. Sheng, W. H. Song, X. B. Zhu, and Y. P. Sun, Appl. Phys. Lett. **112**, 072405 (2018).

[57] X. Zhang, G. Wen, F. Wang, W. Wang, C. Yu, and G. Wu, Appl. Phys. Lett. **77**, 3072 (2000).

[58] K. A. Gschneidner Jr., V. K. Pecharsky, A. O. Pecharsky, and C. B. Zimm, Mater. Sci. Forum **315-317**, 69 (1999).

[59] H. Oesterreicher and F. T. Parker, J. Appl. Phys. **55**, 4334 (1984).

[60] V. Franco, J. S. Blazquez, and A. Conde, Appl. Phys. Lett. **89**, 222512 (2006).

[61] V. Franco and A. Conde, Int. J. Refrig. **33**, 465 (2010).

[62] Y. Su, Y. Sui, J.-G. Cheng, J.-S. Zhou, X. Wang, Y. Wang, and J. B. Goodenough, Phys. Rev. B **87**, 195102 (2013).

[63] W. Liu, J. Zhao, F. Meng, A. Rahman, Y. Qin, J. Fan, L. Pi, Z. Tian, H. Du, L. Zhang, and Y. Zhang, Phys. Rev. B **103**, 214401 (2021).

[64] W. Liu, D. Liang, F. Meng, J. Zhao, W. Zhu, J. Fan, L. Pi, C. Zhang, L. Zhang, and Y. Zhang, Phys. Rev. B **102**, 174417 (2020).

[65] C. Pappas, E. Lelièvre-Berna, P. Falus, P. M. Bentley, E. Moskvin, S. Grigoriev, P. Fouquet, and B. Farago, Phys. Rev. Lett. **102**, 197202 (2009).

[66] A. Hamann, D. Lamago, T. Wolf, H. v. Löhneysen, and D. Reznik, Phys. Rev. Lett. **107**, 037207 (2011).

[67] G. Chang, B. Singh, S.-Y. Xu, G. Bian, S.-M. Huang, C.-H. Hsu, I. Belopolski, N. Alidoust, D. S. Sanchez, H. Zheng, H. Lu, X. Zhang, Y. Bian, T.-R. Chang, H.-T. Jeng, A. Bansil, H. Hsu, S. Jia, T. Neupert, H. Lin *et al.*, Phys. Rev. B **97**, 041104(R) (2018).

[68] M. Neupane, M. M. Hosen, I. Belopolski, N. Wakeham, K. Dimitri, N. Dhakal, J.-X. Zhu, M. Z. Hasan, E. D. Bauer, and F. Ronning, J. Phys.: Condens. Matter **28**, 23LT02 (2016).

[69] Y. Wang, J. H. Yu, Y. Q. Wang, C. Y. Xi, L. S. Ling, S. L. Zhang, J. R. Wang, Y. M. Xiong, T. Han, H. Han, J. Yang, J. Gong, L. Luo, W. Tong, L. Zhang, Z. Qu, Y. Y. Han, W. K. Zhu, L. Pi, X. G. Wan *et al.* Phys. Rev. B **97**, 115133 (2018).